Ti-6Al-4V Hybrid Structure Mechanical Properties – Wrought and Additive Manufactured Powder-Bed Material

O. Dolev*, S. Osovski and A. Shirizly

Faculty of Mechanical Engineering, Technion, Haifa 3200003, Israel

* dolev.ohad@gmail.com

Abstract

The implementation of additive manufacturing techniques in the production of mission critical structural components is challenged by its low throughput and limited build envelope. In recent years, hybrid production methods are emerging to bridge between the build volume and high throughput of conventional production methods and the design freedom enabled by additive manufacturing. The repeatability of material properties and the quality of the interface between the additive manufactured and wrought material are crucial for the adoption of hybrid manufacturing techniques by the industry. Here, the tensile behavior and fracture toughness of a hybrid Ti-6Al-4V alloy are examined in detail. Ti-6Al-4V pre-forms were built onto a wrought Ti-6Al-4V start-plate and extracted via milling. Compact tension and uniaxial tension specimens extracted from the hybrid pre-forms demonstrated good fracture and properties with no preference for crack growth in neither the AM nor wrought materials. Microstructural characterization revealed a 40 mm transition layer into the wrought material which ends abruptly with no evidence of a gradually decaying heat-affected zone. The hybrid manufacturing approach studied here expands the current limitations of large-scale critical components with fine features and allow such structures to be produced with a higher throughput.

Keywords: Additive manufacturing, Hybrid manufacturing, Fracture-toughness, Powder bed

1. Introduction

Titanium and its alloys pose a unique combination of physical and mechanical properties such as high specific strength, high toughness, good corrosion resistance [1–6], etc. As such, Titanium alloys are often found in damage-critical load-bearing structures and weight critical products. Among the various Titanium alloys, Ti-6Al-4V stands out as being one of the most frequently used Titanium alloys in the industry. It is not a surprise then, that with the emergence of additive manufacturing (AM) techniques, Ti-6Al-4V was one of the first metallic material to be incorporated into a commercial critical component [7]. Throughout the development of AM technology, Ti-6Al-4V was studied extensively in the scientific literature [8–17] as well as by aerospace and BioMed industries. Over the last decade, Ti-6Al-4V was intensively integrated into various additive manufacturing processes, demonstrating remarkable business case reasoning through improved functionality, efficient material usage, and cost reduction.

Powder bed additive manufacturing is considered to be a low throughput manufacturing method, with a limited build envelope, thus landing itself mostly for the production of high-quality structures with fine features, very thin walls, lattice structures, fine internal channels, and cavities. In recent years, Hybrid AM - conventional manufacturing processes are emerging as a viable way to overcome the build limitations of AM, thus enhancing the functionally and expanding reach of the AM technology [18,19]. Hybrid manufacturing processes pose a significant technological advance, allowing for component repairs [20–23], production of bi-materials [24–28], and manufacturing of large components with intricate designs [29–33]. Hybrid manufacturing techniques, consisting of both powder bed fusion and wire arc AM hold a promise to result in a manufacturing method which marks the benefits of both worlds, i.e. relative freedom of design along with rapid manufacturing process [34]

With the growing interest in AM of metallic components, the mechanical properties resulting from various powder bed and direct energy deposition techniques have been extensively studied in the literature. As can be observed from [35,36] and references within, both the static (e.g. tensile strength, elongation to failure, etc.) properties, as well as mechanical anisotropy, fracture toughness, and fatigue life, are highly dependent on the process parameters and has been studied extensively. However, for Hybrid manufactured components, the majority of works cited above, have focused on the microstructural characterization and uniaxial tension behavior solely (e.g. [34,37]). Only a few works have studied the fracture properties of Hybrid structures [11,38].

The work presented here is aimed at characterizing the fracture toughness of a Hybrid Ti-6Al-4V structure, produced via selective laser melting (SLM) and subtractive manufacturing of the base plate (wrought Ti-6Al-4V) on which it was manufactured. The rest of the paper is organized as follows: We first describe the experimental procedure by which the hybrid structure was fabricated along with a description of the experimental approach. Next, the microstructure surrounding the AM-Wrought interface is presented along with the measured hardens variations and a detailed defect analysis. The uniaxial mechanical behavior and fracture toughness of the Hybrid material is then compared to those of the wrought and AM material, demonstrating the feasibility of the proposed manufacturing route for load bearing, damage critical components. The main findings of the work are then briefly summarized.

2. Experimental

2.1 Specimens fabrication

An EOS M280 powder bed SLM was used to build a series of pre-forms designated for tensile tests (round rods) and fracture toughness evaluation (cubes). The pre-forms were fabricated from a 30-microns Ti-6Al-4V powder supplied by TLS Technik GmbH. Both the powder and build plate were used in their virgin form i.e. have not experienced any prior heat cycle. The process parameters are given in Table 1. The substrate material for the hybrid specimens manufacturing was wrought chosen to be Ti-6Al-4V cold-rolled plate purchased from TITANIUM INTERNATIONAL GROUP SRL. No support structures were used in the building process to facilitate the mechanical evaluation of the hybrid material. The various pre-forms used for this study and their designation are given in Figure 1 along with an illustration of the tensile and compact-tension fracture specimens overlaid on the pre-forms.

Table1: SLM process parameters

Power	Scan speed	Hatch distance	Hatching strategy
175W	1250 mm/sec	0.012mm	Line

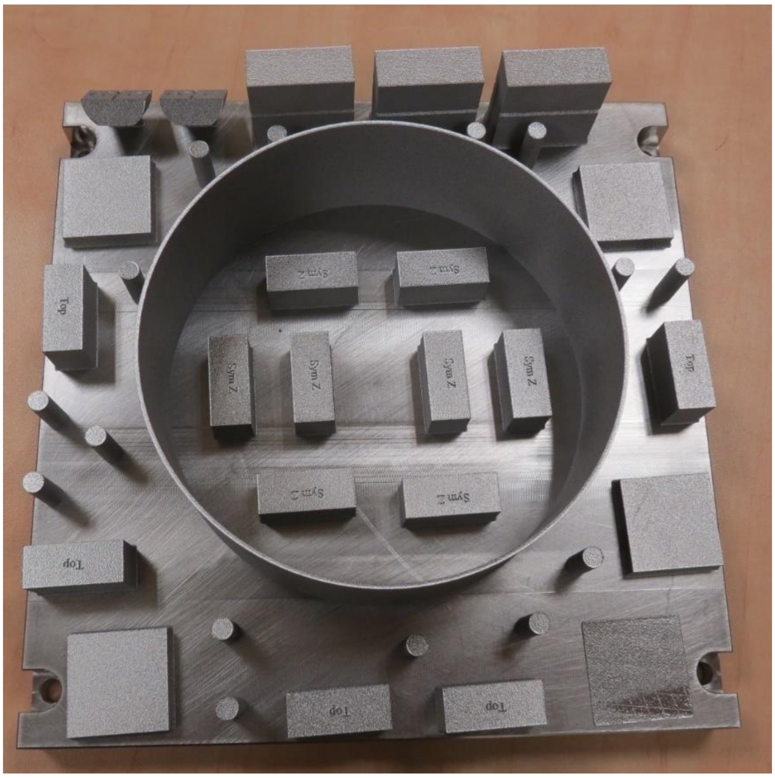

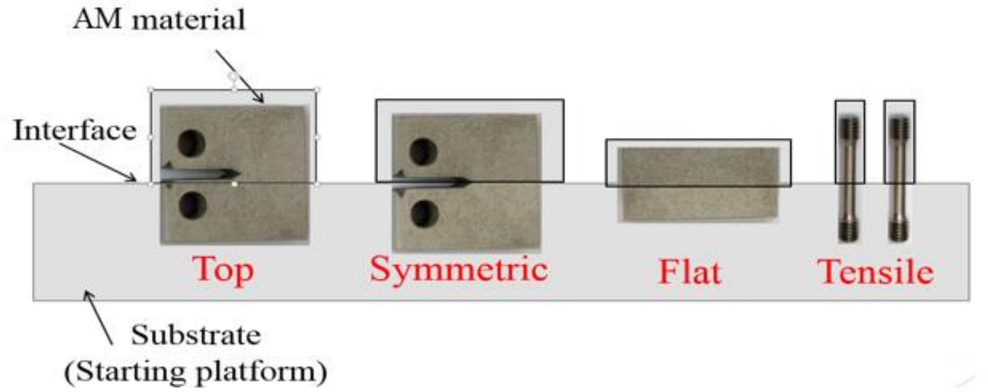

Figure 1: Built pre-forms (AM) on the wrought Ti-6Al-4V substrate plate (top) and an illustration of the pre-forms overlaid with the specimens before post-processing (bottom).

Following the SLM process pre-forms were carefully machined out of the substrate plate and AM material. The pre-forms from the three groups (i.e. hybrid, AM and wrought) were heat-treated following two commonly used stress-release procedures for AM Ti-6Al-4V, namely: 650°C for 3h or 800°C for 4h. Both heat treatments were held and cooled in vacuumed furnace. Finally, the pre-forms were machined into tensile specimens (Figure 2a, in accordance with ASTM E8) and compact-tension (CT) specimen (Figure 2b, following ASTM E399-17). The tensile specimen's geometry was selected to comply with the geometrical limitations induced by the plate thickness. Special care was taken while machining the specimens to ensure that the AM-wrought interface is located at:

i. The center of the gauge for the tensile specimens.
ii. Bellow the notch tip and parallel to the CT specimen's symmetry plane (designated as "Top")
iii. Directly ahead of the notch tip and along the CT specimen's symmetry plane (designates "Symmetric").
iv. Halfway through-thickness of the CT specimen, perpendicular to the crack growth direction (designated "Flat")

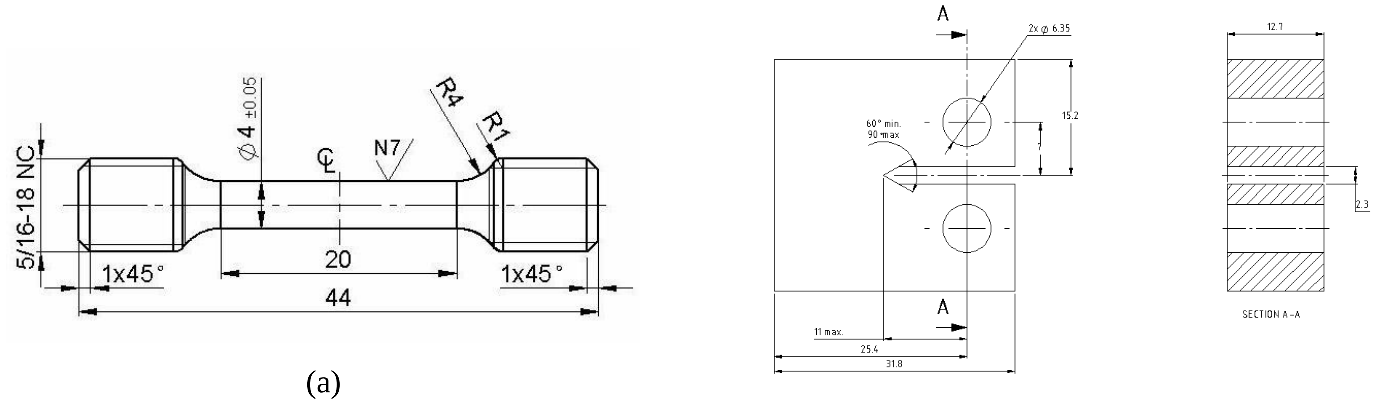

(a)

(b)

Figure 2: (a) ASTM E8 tensile specimen's geometry and dimensions. (B) ASTM E399-17 CT specimen's geometry and dimensions.

In addition to the Hybrid specimens, tensile and CT specimens were machined out of purely AM material (manufactured via the same preforms and on the same plate in the same batch) as well as from the wrought plate serving as substrate. The tensile specimens extracted from the substrate plate (i.e. wrought material). We acknowledge that the tensile test results reported for the wrought material may be different in the rolling direction when compared to the through-thickness direction used for the hybrid specimens. However, through-thickness tensile specimens, complying with the dimensions of ASTM E8 could not be extracted due to the plate thickness.

2.2 Microstructural observations

Hybrid samples were extracted and then grounded and polished using SiC (1000#) followed by colloidal silica (0.04 microns). The polished specimens were lightly etched by swabbing with Kroll's reagent to expose the underlying microstructure. An Olympus BX-51 optical microscope and a high-resolution TESCAN MIRA-3 FEG-SEM were used to study the microstructure surrounding the interface.

Nondestructive testing using Micro-focus Computerized Tomography scanner (Nikon XT H 320 CT Scanning system with a 225 kV micro-focus source, equipped with a reflection target), was used to assess the porosity levels as discussed in Section 3.

2.3 Mechanical testing

Vickers micro-hardness testing was done using Shimadzu HMV-G20 operating at a load of 500gfr.

The tensile tests were carried out using a 100KN Instron tensile machine at a strain rate of $7x10^{-3}$ s^{-1}. Displacement in the AM and wrought tensile experiments were measured using a 25 mm mechanical extensometer (Instron). For the Hybrid tensile tests, prior to conducting the experiments, a black and white speckle pattern was applied via an airbrush and imaged to extract the displacements along the specimen's gage using GOM-ARAMIS digital image correlation (DIC) software.

The compact tension specimens were first fatigue pre-cracked using an Instron 8801 testing machine (Dynacell, Dynamic Load Cell +/- 100 kN) under load control with a sinusoidal waveform in the air at 22±3°C @ 15 Hz. The cyclic loading of the fatigue pre cracking was applied with a load ratio of R=0.1 and a maximum load of 3 kN (200-500K cycles). The maximum stress intensity in the terminal (2.5 %) stage of fatigue crack growth did not exceed 80 % of the KIC value. The crack propagation was monitored using a crack opening displacement gage (COD gage) and visually monitoring the crack growth on the sides of the specimens.

3. Results and discussion

3.1 Microstructural observations

An optical microscope image of the AM-wrought microstructure is presented in Figure 3 for a hybrid specimen subjected to a stress release heat treatment at 800°C for 4 hours. As evident from Figure 3, the microstructural anisotropy, typical of Ti-6Al-4V manufactured by powder bed fusion, is still present after the selected heat treatment. We attribute this to the heat treatment temperature which is well below the beta-transus, with little effect on the columnar prior β boundaries [39] .

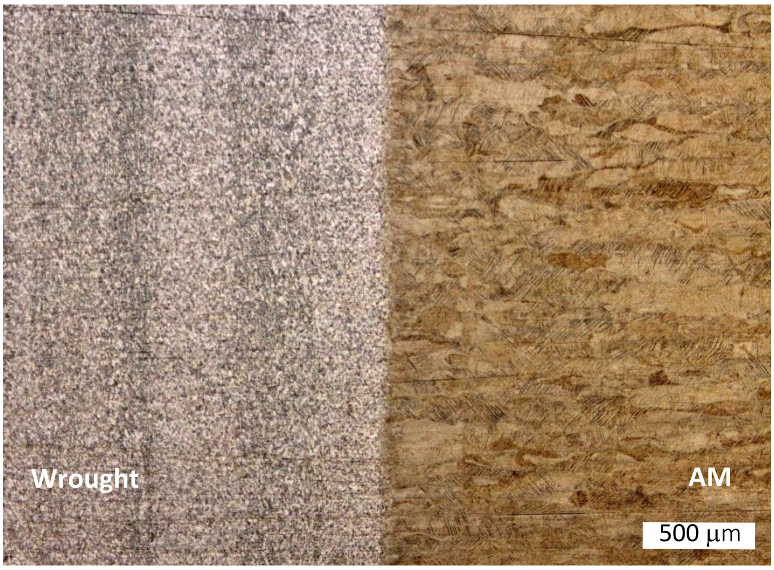

Figure 3: Optical microscopy image of the AM-wrought interface taken at a magnification of 5X

In Figure 4., SEM images of the AM-wrought interface, taken at three magnifications (view fields of 20µm, 120µm, and 250µm) are presented for a hybrid specimen stress-released at 800°C for 4 hours. No porosity or other discontinuities were observed along the AM-wrought interface. Since the SLM process can be considered as a welding type of manufacturing, in which the powder beads are being welded together, one might expect the resulting microstructure at the AM-wrought interface to be similar to those observed after laser beam welding (LBW) of AM Ti-6Al-4V to its wrought counterpart (e.g. [40]). Surprisingly, no clear heat-affected zone was observed and the microstructure remained consistent in appearance for both the AM and wrought sides, with only a thin layer separating them. Unlike the common continuous change in microstructure which is typical of HAZ, the observed layer appears to be consistent and ends abruptly (at least at the magnifications considered in this work).

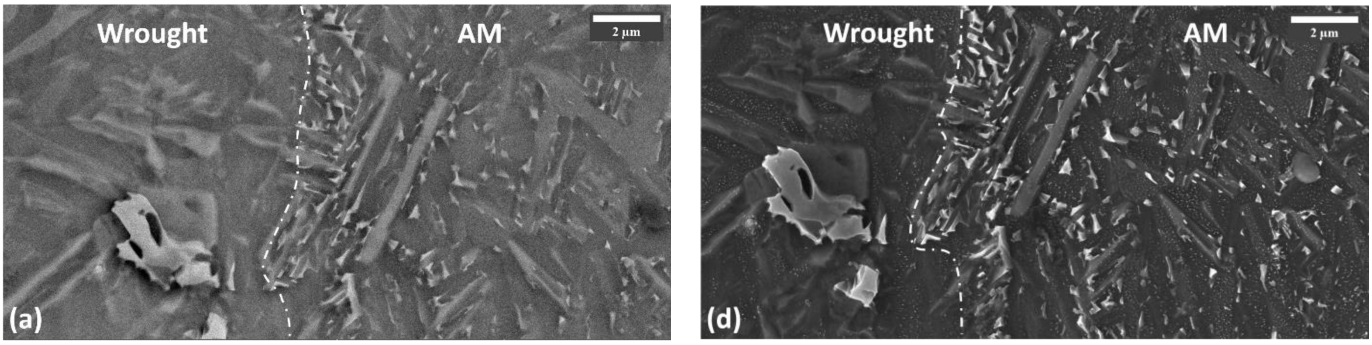

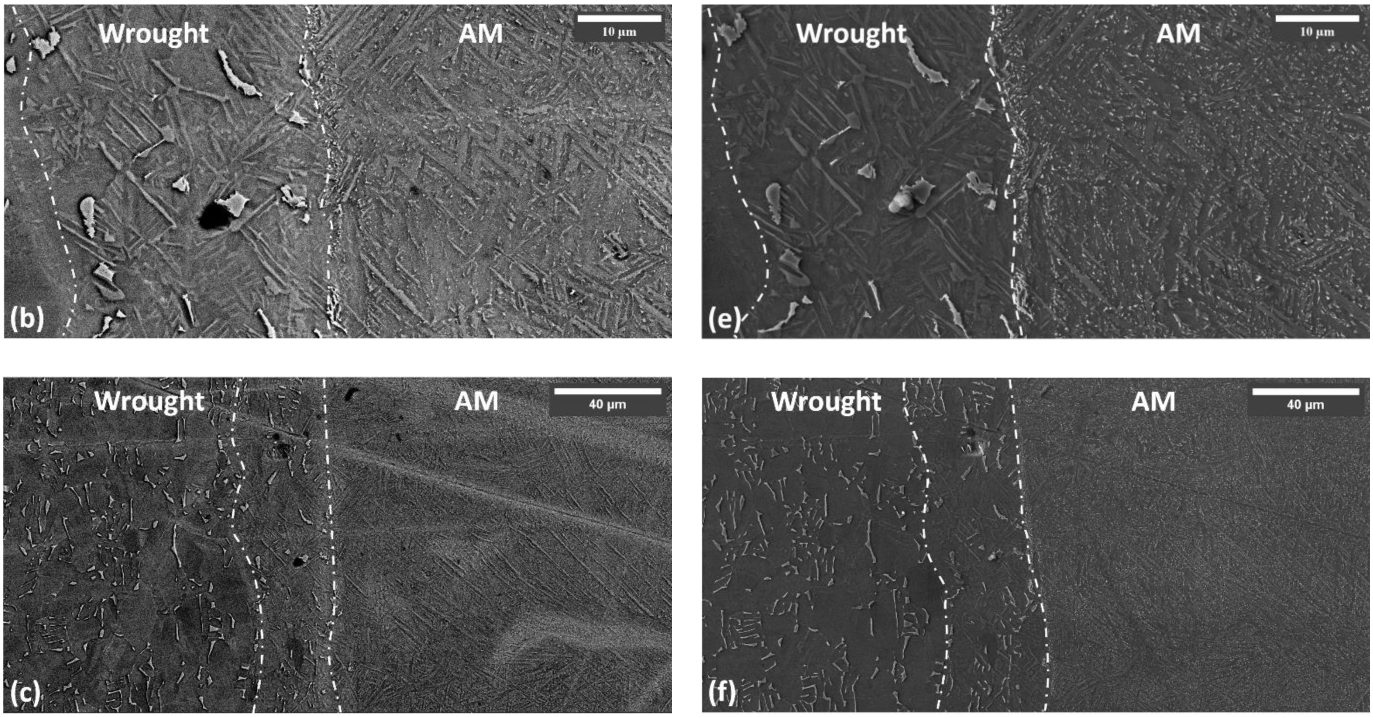

Figure 4: Secondary (left) and Backscattered (right) electron images were taken at the interface of a hybrid specimen heat treated at 800ºC for 4 hours. (a,d) 20μm view field (x27.7K). (b,e) 120μm view field (x4.6k). (c,f) 250μm view field (x2.2k). The interface between the AM and wrought materials, as well as the end of a heat affected zone are marked by dashed lines.

In Figure 4, (b,e) the transition layer can be observed on the wrought side of the specimen. At low magnifications (Figure 4 c&f) the microstructure in the layer resembles the microstructure of the wrought alloy and exhibit the typical $\alpha+\beta$ microstructure. However, under close examination, distinct laths are observed within a layer of ~ 40 μm adjacent to the interface between the wrought and AM materials. These laths are not present anywhere else in the wrought alloy. The area fraction of β grains was measured via image analysis and a slight decrease was observed from 5.8% in the wrought alloy to 4.8% inside the layer (on average). This difference however, when estimated over several regions was found to be statistically insignificant. At this stage we attribute the absence of a HAZ similar to the one observed by Tavlovich et. al. [40] to the thermal cycles experienced by the material throughout the SLM process, however, the full characterization of the microstructural evolution near the interface has to be further studied.

Micro-hardness tests (HV) taken at equal distances from the interface (Figure 5), from both wrought and AM regions, indicate a slight decrease in hardness at a distance of up to 100μm away from the interface for the wrought material, which quickly regains back to typical values of ~348HV . Note however that both materials exhibit a second small drop in hardness at ~900 μm away from the interface.

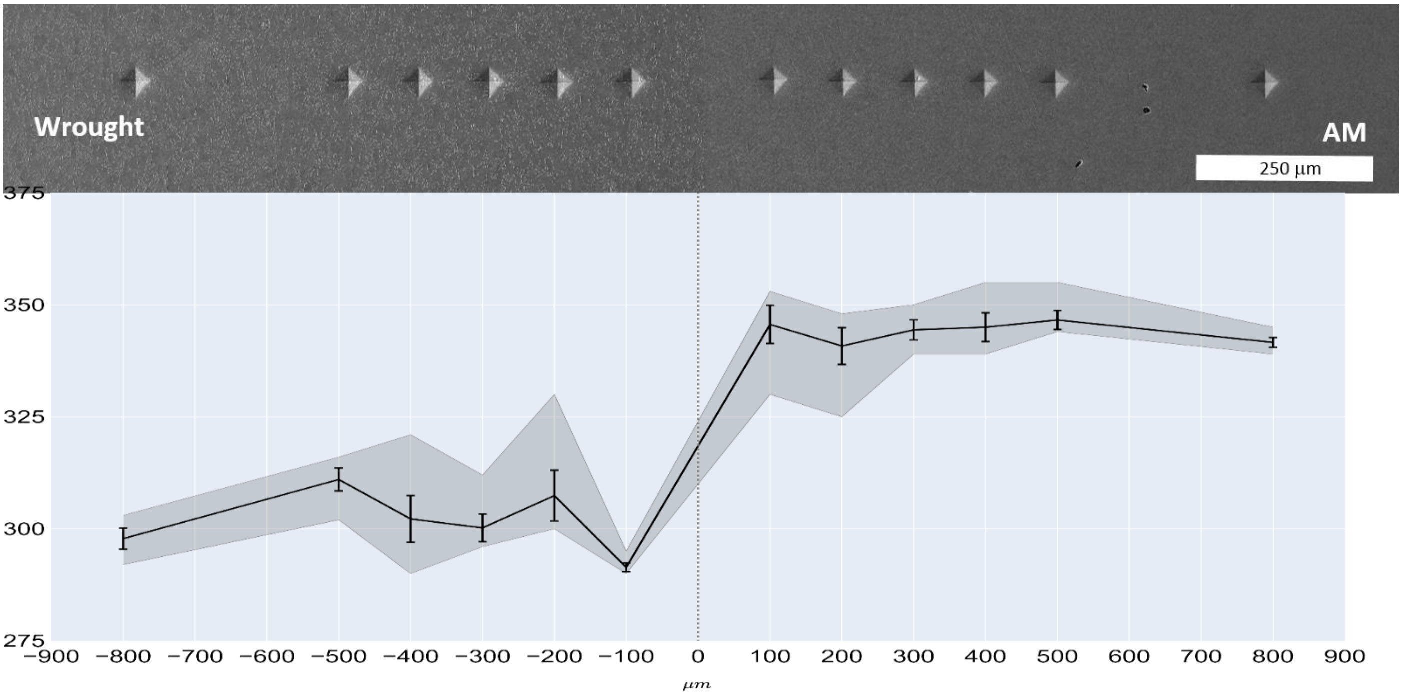

Figure 5: Micro-hardness profile along the longitudinal direction of the hybrid sample as a function of distance from the interface. The grayed region surrounding the mean hardness line marks the full range of measured values for each position.

Unfortunately, we were not able to correlate the lower hardness values with any apparent microstructural variations with the instrumentation at hand.

3.2 Defect analysis

Defect analysis was conducted via a micro-CT apparatus for a cylindrical specimen (Figure 6). The total scanned volume was 602 mm^3. A total of 1109 defects were observed in the AM alloy, while only 755 defects were identified in the wrought alloy, to avoid misidentification resulting from the machine resolution (i.e. a 6µm voxels size) only defects covering at least 8 voxels (2X2X2) were considered in the analysis. Both materials were found to contain less than 0.05% defects in volume. 75% of the defects occupied up to 12 voxels in the AM material, and up to 11 voxels in the wrought alloy. The maximum defect size was found to be 32 voxels for the wrought alloy and 1276 voxels for the AM material. The majority of detectable defects in the AM alloy exhibited an aspect ratio (the ratio of the smallest projection to a major plane to the maximum one) greater than 0.67 with sphericity greater than 0.5, suggesting that the majority of the defects are more likely to be related to gas pores than to lack of fusion. Similar observations were made for the wrought alloy, where the minimum sphericity value was 0.44.

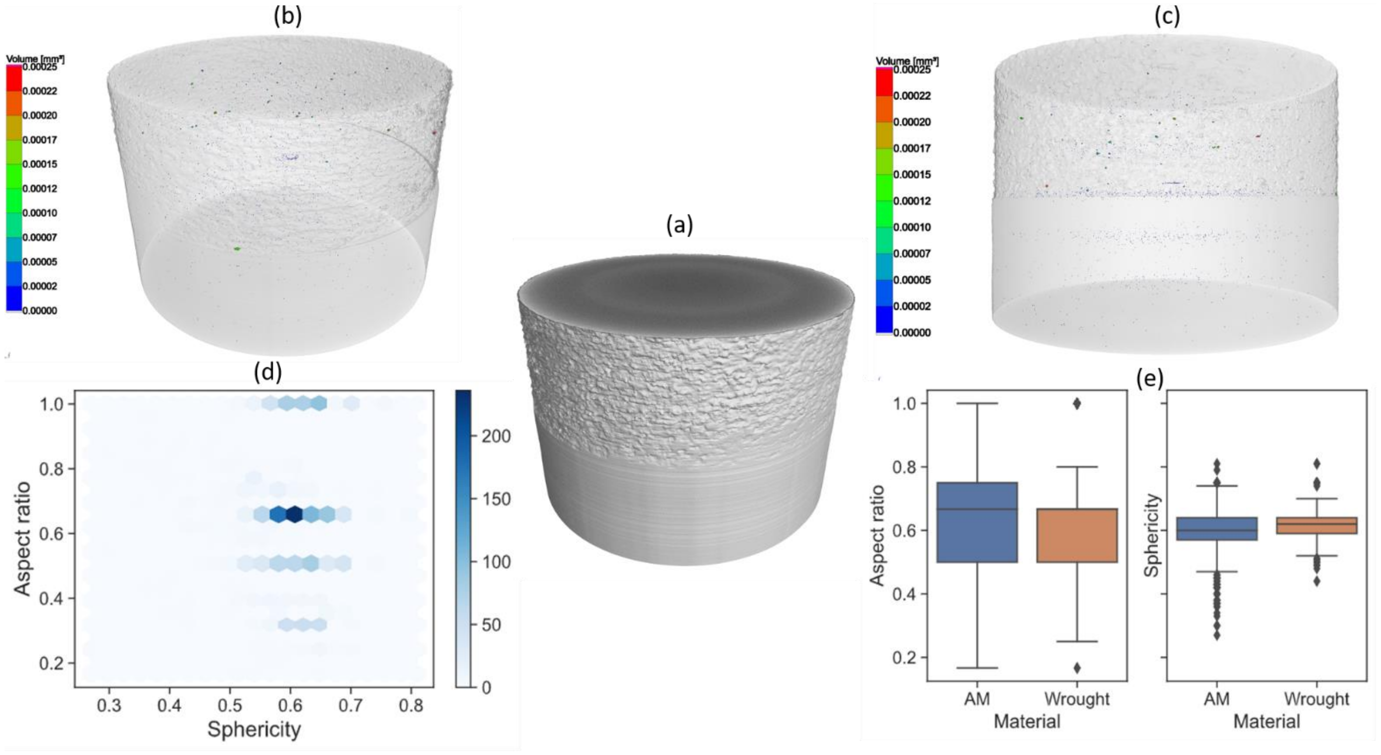

Figure 6: (a) 3D reconstruction of the scanned specimen's outer surface(a) along with detectable defects (b,c). The aspect ratio of the defects and their sphericity is shown for the two materials (c) along with their boxplots (e).

While the mean values of the sphericity are mostly similar between the two materials, as evident from Figure 6e, the outliers in the boxplot created for the AM material span a larger range. The defects diameter, ranges between 17 μm to 262 μm in the AM material and 17 μm to 65 μm in the wrought alloy, with 25% of all defects having a diameter greater than 26 μm in both materials. A parallel coordinate plots is shown in Figure 7 to try and present a more complete picture of the defects found in the micro-CT scans. All of the defects whose volume is greater than 100 $\times 10^{-6}$ mm^3 are found in the AM region, and are characterized by Sphericity lower than 0.5 with 50% being in the range of 0.41 to 0.3. Similarly, their aspect ratio is greater than 0.52 and 50% of them are in the range of 0.76 to 0.88. The rest of the defect characteristics do not exhibit any specific relation with respect to the material they are found in.

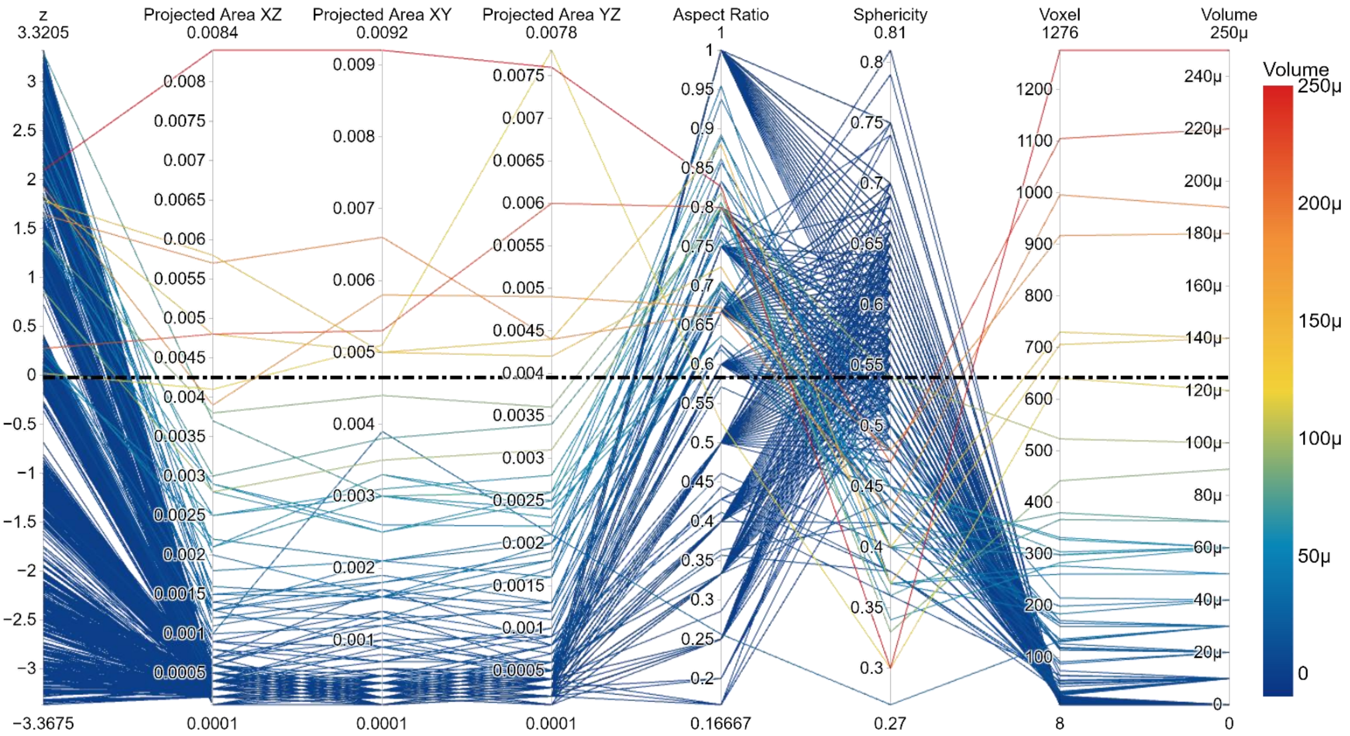

Figure 7: The defects found in the micro-CT scan are mapped on 8 coordinates deemed most relevant. The dashed black line marks the boundary between the wrought alloy (negative z values) and the AM material (positive z values). The color coding is indicative of the defect volume.

The maximum defect volume found in the wrought alloy was v=10 x10^{-6} mm^3. Focusing attention on the few larger defects observed in the AM material , and looking at their distribution along the radial coordinates, it appears that they are mostly present close to the outer surface of the specimen (Figure 8), making them potentially preferred sites for fatigue failure. Interestingly, while larger volume defects appear mostly on the outer part of the specimen, defects with large diameter tend to be present more uniformly across the cross section (Figure 8). Additionally, it appears that the correlation between defect volume and diameter is weak and the larger defect in term of diameter has relatively low volume and vice versa. The two parameters seem to be correlated only for small defects (Figure 8c). We find it encouraging that no evidence was collected during this study to suggest that the AM-wrought interface is more susceptible to defects than the rest of the AM material.

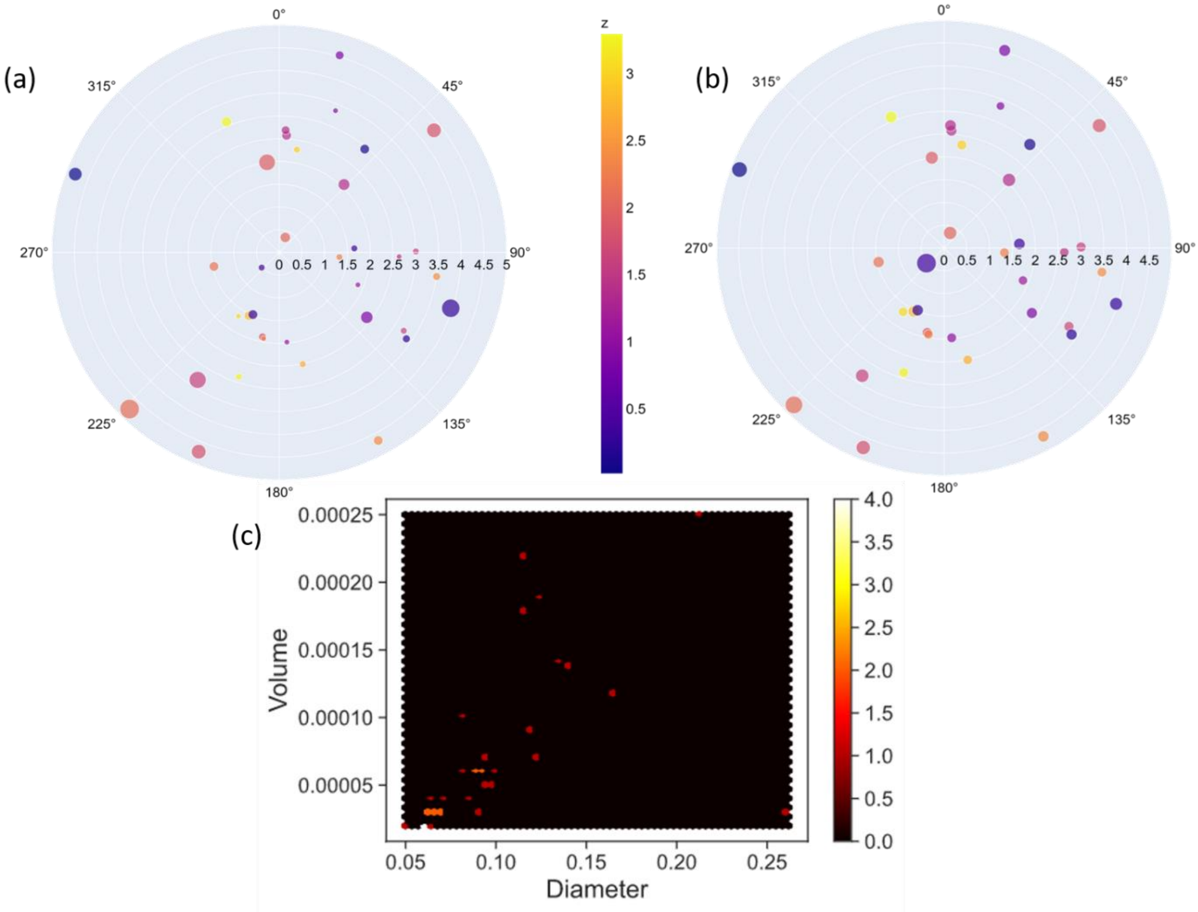

Figure 8: Polar plots showing the distribution of the largest defects in the AM material at the specimen cross section. Values along the build direction (z) are denoted by the marker color while marker size represent the defect diameter (a) and volume (b). A hexbin plot (c) is shown to demonstrate the relation between the large defects in terms of volume and diameter. The color of each bin is a measure to the number of defects contained in it.

Despite the rapid progress made in the field of AM metals, additively manufactured components are still treated with caution when used in scenarios where dynamic loads are applied. The different defects associated with this manufacturing route are known to degrade the fatigue life, while their statistical nature in terms of size shape and location leads to a large scatter and makes it harder to predict the fatigue life using well established models such as NASGRO. Murakami's method [41] has been successfully adopted to describe the effect of defects in AM components in terms of the defects' effective area projected perpendicular to the loading direction [42]. The so called $\sqrt{area}$ parameter, along with the defects sphericity, diameter and location with respect to free surfaces, was shown to be crucial for ensuring usable fatigue life and their prediction via a damage tolerance approach [43]. The relationship between the defects volume, diameter and their projections on the 3 planes (XY;XZ;YZ) is given in Figure 9. It appears that the large defects are mostly isotropic in terms of their projected area, and while there is a correlation between the defects volume and its projected area, some defects with rather large diameter and low volume are present with a much smaller volume. In the context of the work presented here, being the mechanical behavior of hybrid manufactured components, no correlation was found between the presence of the AM-wrought interface and large volume/diameter defects. In fact, as evident in the data presented in this section, the more “dangerous” defects, appear mostly at the bulk of the AM part of the specimen. The presence of some of the larger pores near the specimens surface however is to be taken under notice in future process parameters selection as to avoid the near surface large defects observed in Figure 8.

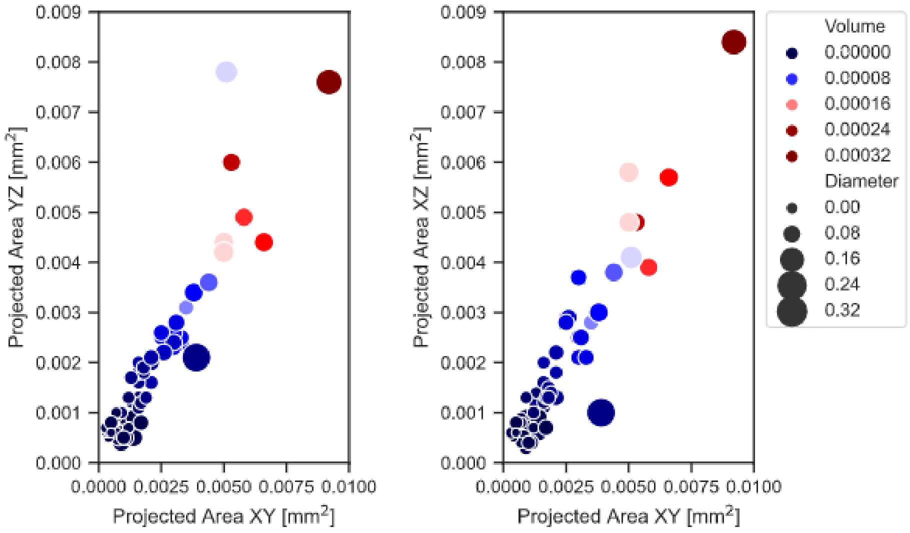

Figure 9: The correlation between the projected area of the largest defects on the three planes XY; XZ; YZ along with their respective volume and diameter.

3.3 Uniaxial tensile tests

All three groups of tensile specimens (i.e. AM; wrought; hybrid) were tested under uniaxial tension. Two series of measurements were conducted for the AM and wrought groups of specimens, each corresponding to one of the heat treatments described above (i.e. 800°C for 4h and 650°C for 3h). The number of (successful) tests performed for each condition is summarized in Table 2 along with the average measured properties and standard errors.

Table 2: Summary of tensile tests

Sample description	**Number of samples**	**Yield stress [MPa]**		**Ultimate Tensile Strength [MPa]**		**Elongation [%]**		**Reduction of Area [%]**	
SLM; HT - 650°C ; 3h	7	1093	±5.78	1174	±3.86	8.70	±0.87	29.00	±3.1
SLM; HT - 800°C ; 4h	10	904	±2.62	997	±2.5	15.80	±0.85	48.70	±0.57
Wrought; HT - 650°C ; 3h	5	860	±10.51	943	±13.33	14.10	±0.54	33.20	±3.18
Wrought; HT - 800°C ; 4h	5	839	±8.45	928	±6.57	14.00	±0.54	34.60	±5.46
Hybrid; HT - 800°C ; 4h	9	845	±4.87	937	±3.27	11.90	±0.43	31.80	±2.3

As evident from Figure 10, increasing the temperature of the heat treatment from 650^{o}C to 800^{o}C has a very limited effect on the measured properties of the wrought material. On the other hand, the AM material which underwent a heat treatment of 800^{o}C for 4 hours exhibited a ~10% decrease in yield and ultimate tensile stress while almost doubling the elongation to failure and reduction of area. For both heat treatments, the AM material is found to be stronger when compared to the wrought, albeit being less ductile when undergoing the 650^{o}C /3 hours heat treatment.

Following the tensile tests of the wrought and AM materials, it was decided to subject the Hybrid material to the 800^{o}C/4hours treatment for all measurements to come. The tensile tests, conducted on the hybrid material, have demonstrated a yield and ultimate stress values similar to the ones obtained for the wrought material undergoing the same heat treatment. Similarly, the measured reduction of area was found to be the same in the wrought and hybrid specimens' groups. In contrast to the aforementioned material parameters, the elongation to failure was found to be slightly lower in the hybrid material (11.9 ± 1.3 compared to 13 ± 1.2). This close similarity in mechanical properties raises a question as to the role played by the AM side of the hybrid tensile specimen. Moreover, it was observed that in all of the 9 hybrid specimens, necking and failure were observed solely on the wrought side. This observation is illustrated in Figure 10, where two failed hybrid specimens are presented after being ground, polished and etched to expose the microstructure and hence aid in identifying which side belongs to which material as well as the location of the interface.

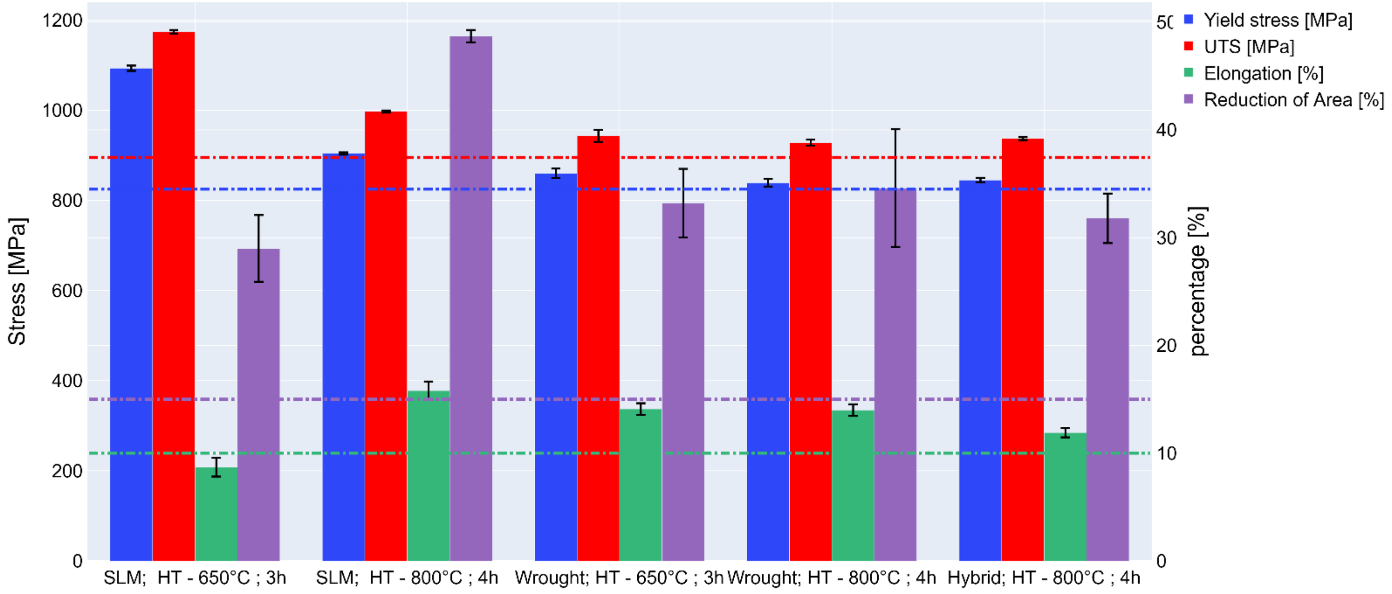

Figure 10: A comparison of the uniaxial tensile test results between the different tested groups. The ASTM F3001 required properties are marked by dashed lines.

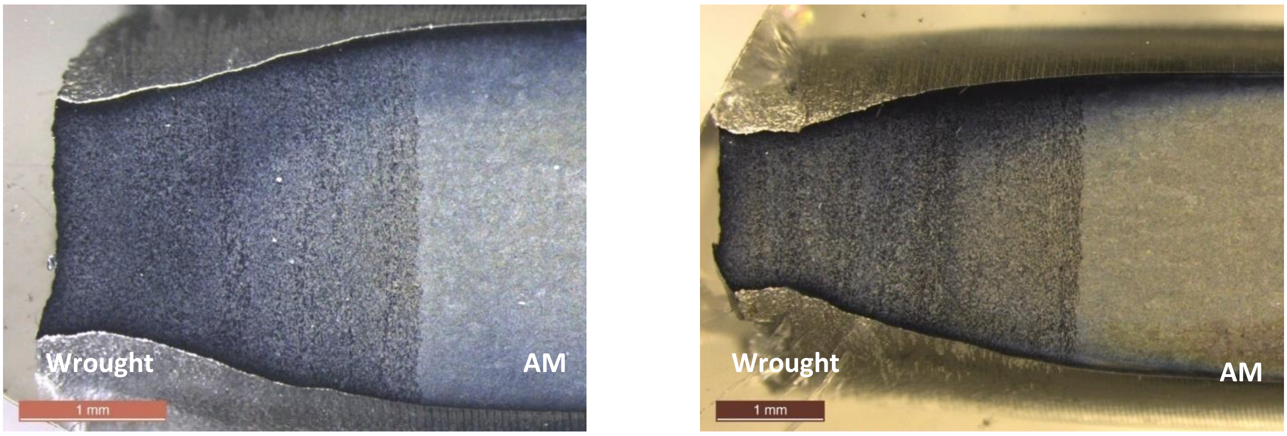

Figure 11: Typical tensile hybrid specimens post-failure. The specimens were ground, polished, and etched to aid in visualizing the location of the interface. Note that necking and failure have occurred in the wrought side and more than 1mm away from the wrought/AM interface.

To further investigate the mechanical behavior under tension of the hybrid specimen, and specifically, the strain partitioning between the two materials composing the hybrid tensile specimen, the strain evolution along the hybrid specimen's gauge section is given in Figure 12. From Figure 11&12 it is clear that while the wrought side of the specimens carries the majority of deformation, its AM counterpart has only yielded to a limited extent. Both SEM and computed x-ray tomography of the failed hybrid specimen did not reveal an increased level of porosity at the AM side of the specimen, in line with the strain measurements and the relatively large distance between the necking region and AM-wrought interface.

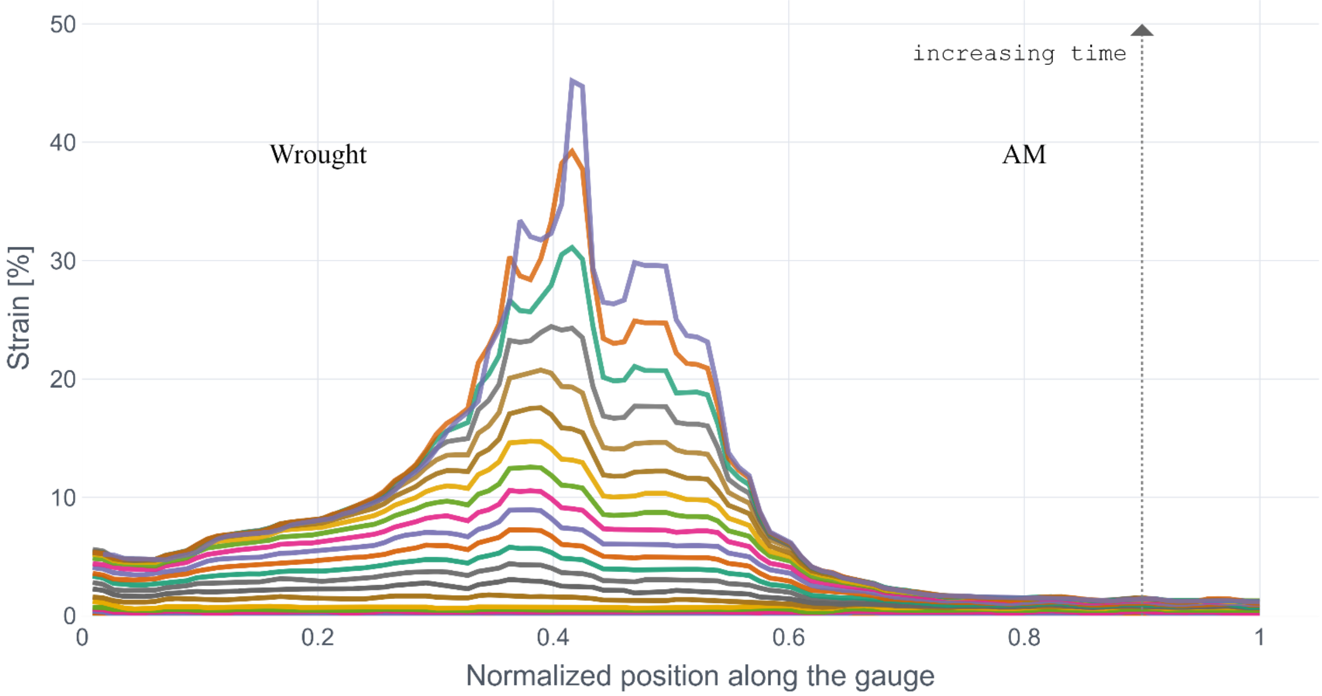

Figure 12: DIC measurements, showing the strain evolution along a path aligned with the tensile direction over time. Note, that since the path over which the strain was extracted is chosen inside the GOM software, the precise allocation of the interface was hard to achieve. Thus, the normalized position does not mean that the interface lies at 0.5 but rather somewhere in its vicinity.

3.4 Fracture toughness

The fracture toughness samples were prepared and tested in accordance with the International Standard Test Method for Linear-Elastic Plane-Strain Fracture Toughness KIC of Metallic Materials ASTM E399-17. The choice of sample geometry (Figure 2b) was somewhat limited due to the geometric restrictions imposed by the wrought plate dimensions and CT25 specimens were extracted from the In-plane direction of the plate. Similar to the testing plan in Section 3.2, the wrought and AM materials were tested for both heat treatments, as to set a baseline for the measurements of the hybrid material. The test groups and number of specimens within each are summarized in Table 3.

Table 3: Fracture toughness results of wrought material, AM and hybrid samples

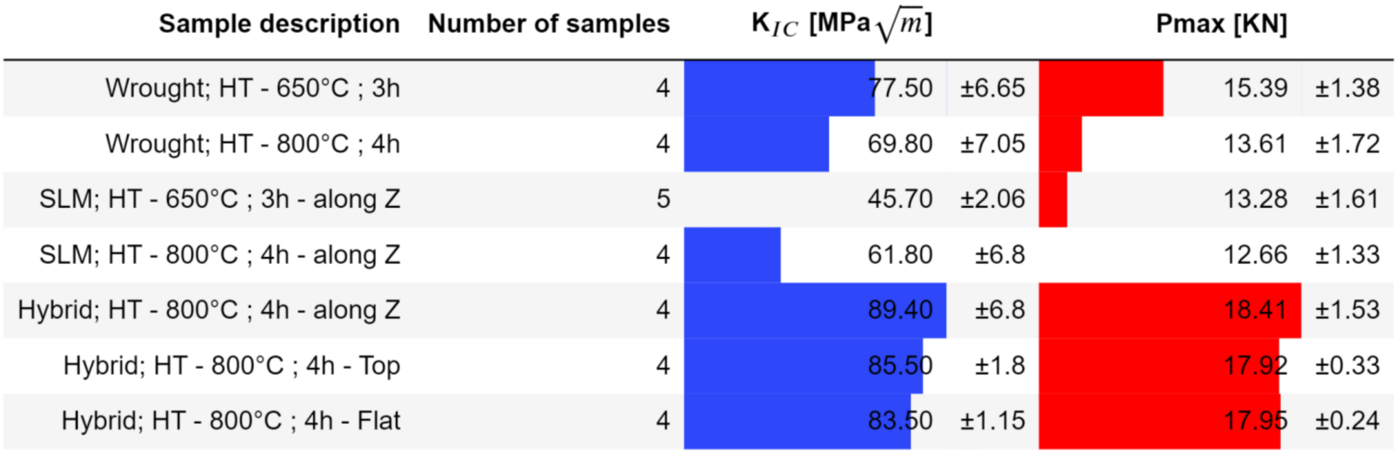

Sample description	Number of samples	K_{IC} [MPa $\sqrt{m}$]		Pmax [KN]	
Wrought; HT - 650°C ; 3h	4	77.50	±6.65	15.39	±1.38
Wrought; HT - 800°C ; 4h	4	69.80	±7.05	13.61	±1.72
SLM; HT - 650°C ; 3h - along Z	5	45.70	±2.06	13.28	±1.61
SLM; HT - 800°C ; 4h - along Z	4	61.80	±6.8	12.66	±1.33
Hybrid; HT - 800°C ; 4h - along Z	4	89.40	±6.8	18.41	±1.53
Hybrid; HT - 800°C ; 4h - Top	4	85.50	±1.8	17.92	±0.33
Hybrid; HT - 800°C ; 4h - Flat	4	83.50	±1.15	17.95	±0.24

While the tensile properties of the wrought material were found to be only weakly sensitive to the choice of heat treatment, the fracture toughness was observed to vary by close to 10% between the two heat treatments, making the 650°C/3h favorable. In the AM, the relative difference between the two test conditions yields a toughening of roughly 26%, in accordance with the improved ductility observed for the tensile tests. It is worth noting that the SLM material's response to the studied heat treatments is exactly opposite to that of the wrought material with 800°C/4h being the preferred heat treatment.

Due to the higher sensitivity of the AM material to the selected heat treatment and the opposite effect the heat treatments have on the measured fracture toughness, the large difference in K_{IC} between the AM and wrought materials resulting from the 650°C/3h treatment (~40%) is considerably reduced for the 800°C/4h (~11%). In order to test the hybrid material at conditions for which its two constituents have similar KIC values, as well to remain consistent with the test program of section 3.2, all of the hybrid fracture specimens were treated at 800°C/4h.

The results of the fracture toughness experiments are summarized in Figure 13. The three groups of hybrid materials, regardless of their orientation, have demonstrated higher fracture toughness (and maximum load) than the specimens belonging to either the AM or wrought category. Here we note, that while we are aware to the fact that the ASTM formula used to calculate K_{IC} from the measured loads during the experiment is invalid for a bi-material[44,45], The relative differences between the two materials hardening curve are not very big and thus we consider the classical equation to be a decent approximation. Nonetheless, even if ignoring the actual K_{IC} values, the maximum loads leading to crack propagation are substantially higher for the hybrid specimens.

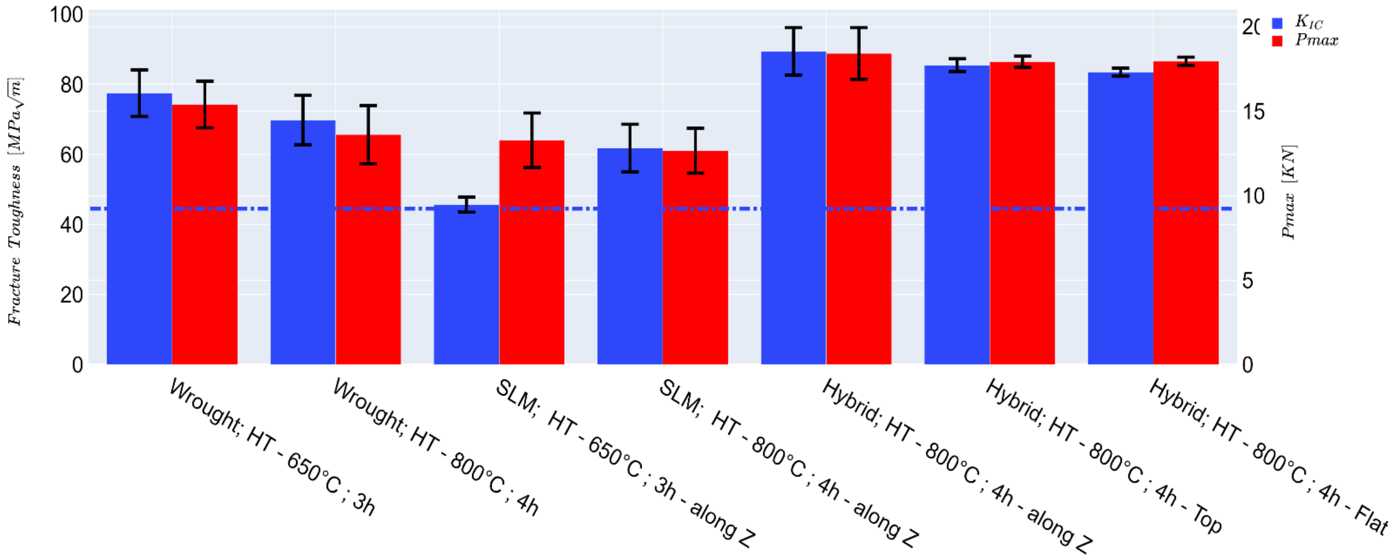

Figure 13: A comparison of the fracture test results between the different tested groups. The dashed line marks the ASTM value of $K_{IC} = 44.5MPa\sqrt{m}$

.

In all of the flat hybrid fracture tests, the fatigue pre-crack was observed to grow in a non-uniform manner (Figure 14), propagating faster in the wrought side during the fatigue pre-cracking process. Nonetheless, No evidence for abrupt crack growth on one of the sides (i.e. AM-wrought) was observed and it appears that the fatigue crack, albeit being non-uniform has grown in a continuous manner. To estimate the toughens in the presence of non-uniform pre-crack fronts, the post-mortem measured fatigue crack length, required for the KIC calculation was determined by averaging the actual crack length taken from five evenly distributed measurement along the crack front. Contradictory to the report of Zhang et al. [11] where the crack growth in a wire arc additive manufactured Ti-6Al-4V hybrid material was observed to grow into the substrate material, here the crack appeared to adhere to the geometrical symmetry plane of the specimen with some undulations between the AM and wrought parts. In [11], the crack path selection was rationalized with respect to the residuals strains which were mapped along the specimen. Also, a clear HAZ was reported near the WAAM-wrought interface. It is plausible that the minor (if any) residual stresses in our hybrid material, in conjunction with the absence of a HAZ are the main cause for the discrepancy between the observations drawn here and in [11].

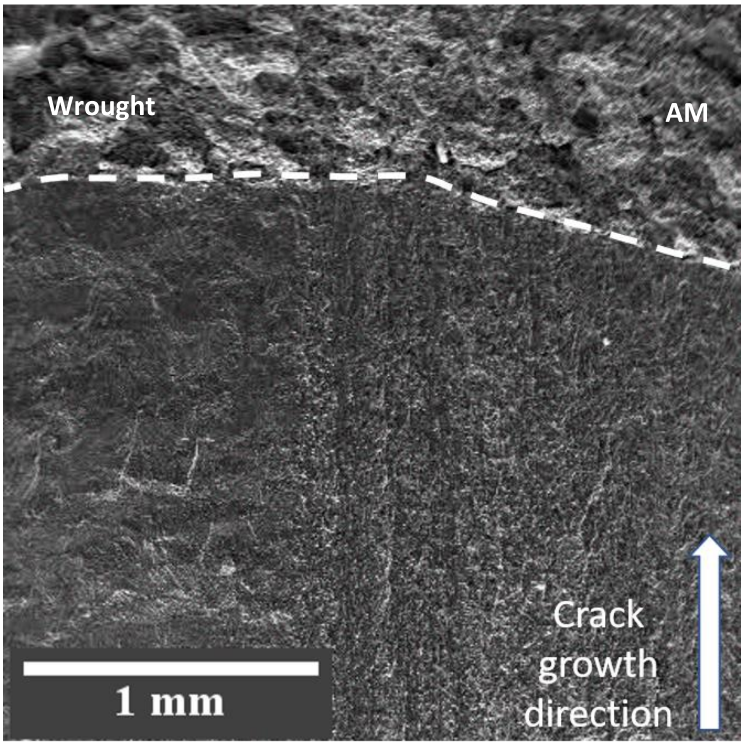

Figure 14: The fatigued pre-crack and final fracture of a flat hybrid specimen. The white dashed line denote the transition from pre-cracking to crack propagation under increasing load.

4. Summary and Conclusions

The feasibility of a hybrid wrought-AM manufacturing route for Ti-6Al-4V damage critical load bearing components was demonstrated through series of experimentation. Hybrid specimens, with their AM part manufactured via SLM were tested for microstructural variations, presence of defects, uniaxial tensile ductility and fracture toughness for several configurations. While defects were found in both the AM part of the specimen and its wrought counterpart, their characteristics were not different from those reported in the literature for other SLM Ti-6Al-4V specimens [43,46,47]. Moreover, the spatial variability of defects did not exhibit any correlation with the location of the AM-wrought interface. In fact, the majority of the more “dangerous” defects were observed to lie mostly at the bulk of the AM region of the specimen, far away from the interface. The combination of a nearly defect free zone (i.e. the wrought alloy) along with a region containing various defects (while still reasonably sized and shaped) can be treated by adopting the Zone-based approach for structural integrity [48]. Following the zone-based approach, one can envision a manufacturing scheme in which a large component is designed via a hybrid route without gepordizing its performance, nor requiring extra NDT measures which are not used in conventional manufacturing techniques.

The microstructure near the interface did not exhibit the typical HAZ often observed in laser welding of AM Ti-6Al-4V to wrought Ti-6Al-4V. Instead, a thin layer, roughly 40μm in width, was observed to extend from the interface into the wrought alloy, were the microstructure evolved from the otherwise α+β structure with equiaxed α grains. The transition layer, is characterized by the appearance of a lath structure, with a marginally lower fraction of β. A full microstructural characterization of the transition layer and its evolution given different heat treatments was outside the scope of this work. However, a deeper understanding of this observation may be transferred into conventional laser welding applications as a mean of achieving better microstructural uniformity.

The uniaxial tensile test results for the hybrid structure, demonstrate lower values of yield and UTS stresses when compared to the purely SLM specimens. They do however exhibit properties (both in terms of stress and ductility) superior to those requires by the ASTM-F3001 standard and thus are considered safe for load bearing applications.

Fracture toughness tests were conducted on hybrid specimens with the initial notch located in different locations and orientations with respect to the AM-wrought interface. The results of the hybrid specimens have shown them to be superior to both the AM and wrought specimens. This observation not only strengthen the usability of the proposed manufacturing method, but it also suggests that the fatigue life of hybrid components can be expected to retain to industrial standards. However, since no fatigue life estimation was done in this work this point is left open for future study.

The main findings of this work are:

- The hybrid specimens did not exhibit any type of defects in the vicinity of the interface. Furthermore, the micro-hardness values were recovered to those expected from the individual materials within 100μm for the case of the wrought alloy and 200μm for the AM one.
- The HAZ typically associated with laser welding of Ti-6Al-4V was not observed for the hybrid material, presumably due to the diminishing heating cycles associate with the AM process and their relatively short duration (per cycle).
- The two heat treatments considered in this work, were found to have negligible effect on the tensile properties of the wrought material while drastically improving the tensile ductility of the AM material.
- Hybrid AM-wrought tensile specimens were shown to localize the majority of deformation in the wrought material with little to no plasticity observed in its AM counterpart.

- The fracture toughness of AM and wrought samples was observed to react in an opposing trend when subjected to the same heat treatments. At this stage this is merely an observation, but one which merits further investigation.
- It was found that the fracture toughness of the hybrid material is superior to that of either the AM or the wrought alloy. The unique crack tip constrains emerging at a bi-material interface are not sufficient to explain this observation as this observation prevailed also for the “Flat” and “Top” specimens at which crack propagation was not along the interface.

To summarize, we have shown that *Hybrid manufacturing of load-bearing, damage-critical, Ti-6Al-4V components, is indeed a viable option*. While their fatigue tolerance is yet to be investigated, both the tensile and fracture toughness results are extremely promising. During this investigation, several peculiarities, which we did not anticipate a-priori have been observed. Despite the vast body of knowledge gathered in recent years regarding the differences between wrought and AM Ti-6Al-4V, we are not aware of any publication in which the opposite trends we identified were previously emphasized and explored.

5. Acknowledgements

The authors would like to acknowledge the assistance of the technical staff in the Israel Institute of Metallurgy at the Technion – Israel Institute of Technology and the Materials Processing group at Rafael Metal Technology Center for their technical assistance along this work. S.O would like to gratefully acknowledge the financial support provided by the Pazy foundation through the young researchers award Grant #1176.

6. References

[1] G. Welsch, R. Boyer, E.W. Collings, Materials properties handbook: titanium alloys, ASM international, 1993.

[2] C. Leyens, M. Peters, Titanium and titanium alloys: fundamentals and applications, John Wiley & Sons, 2003.

[3] G. Lütjering, J.C. Williams, Titanium, Springer Science & Business Media, 2007.

[4] P. Singh, H. Pungotra, N.S. Kalsi, On the characteristics of titanium alloys for the aircraft applications, Mater. Today Proc. 4 (2017) 8971–8982.

[5] A. Leon, G.K. Levy, T. Ron, A. Shirizly, E. Aghion, The effect of hot isostatic pressure on the corrosion performance of Ti-6Al-4V produced by an electron-beam melting additive manufacturing process, Addit. Manuf. (2020) 101039.

[6] A. Leon, G.K. Levy, T. Ron, A. Shirizly, E. Aghion, The effect of strain rate on stress corrosion performance of Ti6Al4V alloy produced by additive manufacturing process, J. Mater. Res. Technol. (2020).

[7] B.P. Conner, G.P. Manogharan, A.N. Martof, L.M. Rodomsky, C.M. Rodomsky, D.C. Jordan, J.W. Limperos, Making sense of 3-D printing: Creating a map of additive manufacturing products and services, Addit. Manuf. 1 (2014) 64–76.

[8] B. Dutta, F.H.S. Froes, The additive manufacturing (AM) of titanium alloys, in: Titan. Powder Metall., Elsevier, 2015: pp. 447–468.

[9] S. Leuders, M. Thöne, A. Riemer, T. Niendorf, T. Tröster, H.A. a Richard, H.J. Maier, On the mechanical behaviour of titanium alloy TiAl6V4 manufactured by selective laser melting: Fatigue resistance and crack growth performance, Int. J. Fatigue. 48 (2013) 300–307.

[10] P. Edwards, M. Ramulu, Effect of build direction on the fracture toughness and fatigue crack growth in selective laser melted Ti-6Al-4 V, Fatigue Fract. Eng. Mater. Struct. 38 (2015) 1228–1236.

[11] J. Zhang, X. Zhang, X. Wang, J. Ding, Y. Traoré, S. Paddea, S. Williams, Crack path selection at the interface of wrought and wire+ arc additive manufactured Ti--6Al--4V, Mater. Des. 104 (2016) 365–375.

[12] P. Kumar, U. Ramamurty, Microstructural optimization through heat treatment for enhancing the fracture toughness and fatigue crack growth resistance of selective laser melted Ti6Al4V alloy, Acta Mater. 169 (2019) 45–59.

[13] R. Fadida, A. Shirizly, D. Rittel, Dynamic tensile response of additively manufactured Ti6Al4V with embedded spherical pores, J. Appl. Mech. 85 (2018).

[14] A.H. Chern, P. Nandwana, T. Yuan, M.M. Kirka, R.R. Dehoff, P.K. Liaw, C.E. Duty, A review on the fatigue behavior of Ti-6Al-4V fabricated by electron beam melting additive manufacturing, Int. J. Fatigue. 119 (2019) 173–184. https://doi.org/10.1016/j.ijfatigue.2018.09.022.

[15] L. Novotný, M. Béreš, H.F.G. de Abreu, J. Zajac, W. Bleck, Thermal analysis and phase transformation behaviour during additive manufacturing of Ti–6Al–4V alloy, Mater. Sci. Technol. (United Kingdom). 35 (2019) 846–855. https://doi.org/10.1080/02670836.2019.1593669.

[16] C. Chen, Y. Xie, X. Yan, S. Yin, H. Fukanuma, R. Huang, R. Zhao, J. Wang, Z. Ren, M. Liu, H. Liao, Effect of hot isostatic pressing (HIP) on microstructure and mechanical properties of Ti6Al4V alloy fabricated by cold spray additive manufacturing, Addit. Manuf. 27 (2019) 595–605. https://doi.org/10.1016/j.addma.2019.03.028.

[17] S. Liu, Y.C. Shin, Additive manufacturing of Ti6Al4V alloy: A review, Mater. Des. 164 (2019) 107552. https://doi.org/10.1016/j.matdes.2018.107552.

[18] M. Merklein, D. Junker, A. Schaub, F. Neubauer, Hybrid additive manufacturing technologies - An analysis regarding potentials and applications, Phys. Procedia. 83 (2016) 549–559. https://doi.org/10.1016/j.phpro.2016.08.057.

[19] B. Nau, A. Roderburg, F. Klocke, Ramp-up of hybrid manufacturing technologies, CIRP J. Manuf. Sci. Technol. 4 (2011) 313–316. https://doi.org/10.1016/j.cirpj.2011.04.003.

[20] L. Li, Repair of directionally solidified superalloy GTD-111 by laser-engineered net shaping, J. Mater. Sci. 41 (2006) 7886–7893. https://doi.org/10.1007/s10853-006-0948-0.

[21] J. Song, Q. Deng, C. Chen, D. Hu, Y. Li, Rebuilding of metal components with laser cladding forming, Appl. Surf. Sci. 252 (2006) 7934–7940. https://doi.org/10.1016/j.apsusc.2005.10.025.

[22] L. Sexton, S. Lavin, G. Byrne, A. Kennedy, Laser cladding of aerospace materials, J. Mater. Process. Technol. 122 (2002) 63–68. https://doi.org/10.1016/S0924-0136(01)01121-9.

[23] D.D. Gill, J.E. Smugeresky, M.F. Harris, C. V Robino, M.L. Griffith, On the Interface Between LENS®Deposited Stainless Steel 304L Repair Geometry and Cast or Machined Components, Sandia Rep. (2004).

[24] H. Kim, W. Cong, H.-C. Zhang, Z. Liu, Laser engineered net shaping of nickel-based superalloy Inconel 718 powders onto AISI 4140 alloy steel substrates: Interface bond and fracture failure mechanism, Materials (Basel). 10 (2017) 341.

[25] C. Tan, K. Zhou, W. Ma, L. Min, Interfacial characteristic and mechanical performance of maraging steel-copper functional bimetal produced by selective laser melting based hybrid manufacture, Mater. Des. 155 (2018) 77–85. https://doi.org/10.1016/j.matdes.2018.05.064.

[26] E. Cyr, H. Asgari, S. Shamsdini, M. Purdy, K. Hosseinkhani, M. Mohammadi, Fracture behaviour of additively manufactured MS1-H13 hybrid hard steels, Mater. Lett. 212 (2018) 174–177. https://doi.org/10.1016/j.matlet.2017.10.097.

[27] H. Azizi, R. Ghiaasiaan, R. Prager, M.H. Ghoncheh, K.A. Samk, A. Lausic, W. Byleveld, A.B. Phillion, Metallurgical and mechanical assessment of hybrid additively-manufactured maraging tool steels via selective laser melting, Addit. Manuf. 27 (2019) 389–397.

https://doi.org/10.1016/j.addma.2019.03.025.

[28] S. Shakerin, A. Hadadzadeh, B.S. Amirkhiz, S. Shamsdini, J. Li, M. Mohammadi, Additive manufacturing of maraging steel-H13 bimetals using laser powder bed fusion technique, Addit. Manuf. 29 (2019) 100797. https://doi.org/10.1016/j.addma.2019.100797.

[29] A. Schaub, V. Juechter, R.F. Singer, M. Merklein, Characterization of hybrid components consisting of SEBM additive structures and sheet metal of alloy Ti-6Al-4V, in: Key Eng. Mater., 2014: pp. 609–614.

[30] B. Ahuja, A. Schaub, M. Karg, R. Schmidt, M. Merklein, M. Schmidt, high power laser beam melting of Ti-6Al-4V on formed sheet metal to achieve hybrid structures, in: Laser 3D Manuf. II, 2015: p. 93530X.

[31] F. Huber, T. Papke, M. Kerkien, F. Tost, G. Geyer, M. Merklein, M. Schmidt, Customized exposure strategies for manufacturing hybrid parts by combining laser beam melting and sheet metal forming, J. Laser Appl. 31 (2019) 22318.

[32] L. Butzhammer, P. Dubjella, F. Huber, A. Schaub, M. Aumüller, O. Petrunenko, M. Merklein, M. Schmidt, Experimental investigation of a process chain combining sheet metal bending and laser beam melting of Ti-6Al-4V, Lasers in Manufactuing (LiM). (2017).

[33] C. Tan, K. Zhou, W. Ma, L. Min, Interfacial characteristic and mechanical performance of maraging steel-copper functional bimetal produced by selective laser melting based hybrid manufacture, Mater. Des. 155 (2018) 77–85. https://doi.org/10.1016/j.matdes.2018.05.064.

[34] X. Shi, S. Ma, C. Liu, Q. Wu, J. Lu, Y. Liu, W. Shi, Selective laser melting-wire arc additive manufacturing hybrid fabrication of Ti-6Al-4V alloy: Microstructure and mechanical properties, Mater. Sci. Eng. A. 684 (2017) 196–204.

[35] J.J. Lewandowski, M. Seifi, Metal Additive Manufacturing: A Review of Mechanical Properties, Annu. Rev. Mater. Res. 46 (2016) 151–186. https://doi.org/10.1146/annurev-matsci-070115-032024.

[36] Y. Kok, X.P. Tan, P. Wang, M.L.S. Nai, N.H. Loh, E. Liu, S.B. Tor, Anisotropy and heterogeneity of microstructure and mechanical properties in metal additive manufacturing: A critical review, Mater. Des. 139 (2018) 565–586. https://doi.org/10.1016/j.matdes.2017.11.021.

[37] Y. Zhu, J. Li, X. Tian, H. Wang, D. Liu, Microstructure and mechanical properties of hybrid fabricated Ti-6.5Al-3.5Mo-1.5Zr-0.3Si titanium alloy by laser additive manufacturing, Mater. Sci. Eng. A. 607 (2014) 427–434. https://doi.org/10.1016/j.msea.2014.04.019.

[38] J. Zhang, X. Wang, S. Paddea, X. Zhang, Fatigue crack propagation behaviour in wire+arc additive manufactured Ti-6Al-4V: Effects of microstructure and residual stress, Mater. Des. 90 (2016) 551–

561. https://doi.org/10.1016/j.matdes.2015.10.141.

[39] X.Y. Zhang, G. Fang, S. Leeflang, A.J. Böttger, A. A. Zadpoor, J. Zhou, Effect of subtransus heat treatment on the microstructure and mechanical properties of additively manufactured Ti-6Al-4V alloy, J. Alloys Compd. 735 (2018) 1562–1575. https://doi.org/10.1016/j.jallcom.2017.11.263.

[40] B. Tavlovich, A. Shirizly, R. Katz, EBW and LBW of additive manufactured Ti6Al4V products, Weld J. 97 (2018) 179S--190S.

[41] Y. Murakami, M. Endo, Effects of defects, inclusions and inhomogeneities on fatigue strength, Int. J. Fatigue. 16 (1994) 163–182. https://doi.org/10.1016/0142-1123(94)90001-9.

[42] Y. Yamashita, T. Murakami, R. Mihara, M. Okada, Y. Murakami, Defect analysis and fatigue design basis for Ni-based superalloy 718 manufactured by selective laser melting, Int. J. Fatigue. 117 (2018) 485–495. https://doi.org/10.1016/j.ijfatigue.2018.08.002.

[43] N. Sanaei, A. Fatemi, Defects in Additive Manufactured Metals and Their Effect on Fatigue Performance: A State-of-the-Art Review, Prog. Mater. Sci. (2020) 100724. https://doi.org/10.1016/j.pmatsci.2020.100724.

[44] H. Lee, Y. Kim, Interfacial crack-tip constraints and J -integral for bi-materials with plastic hardening mismatch, Int. J. Fract. (2007) 231–243. https://doi.org/10.1007/s10704-006-9025-6.

[45] C.F. Shih, Cracks on bimaterial interfaces : elasticity and plasticity aspects, Mater. Sci. Eng. A. 143 (1991) 77–90.

[46] A. du Plessis, I. Yadroitsava, I. Yadroitsev, Effects of defects on mechanical properties in metal additive manufacturing: A review focusing on X-ray tomography insights, Mater. Des. 187 (2020) 108385. https://doi.org/10.1016/j.matdes.2019.108385.

[47] Y.N. Hu, S.C. Wu, P.J. Withers, J. Zhang, H.Y.X. Bao, Y.N. Fu, G.Z. Kang, The effect of manufacturing defects on the fatigue life of selective laser melted Ti-6Al-4V structures, Mater. Des. 192 (2020). https://doi.org/10.1016/j.matdes.2020.108708.

[48] M. Gorelik, Additive manufacturing in the context of structural integrity, Int. J. Fatigue. 94 (2017) 168–177. https://doi.org/10.1016/j.ijfatigue.2016.07.005.